Available online at www.sciencedirect.com
SCIENCE DIRECT
Polymer 47 (2006) 5494–5504
polymer
www.elsevier.com/locate/polymer

Polyethylene {201} crystal surface: interface stresses and thermodynamics

Markus Hütter, Pieter J. in 't Veld, Gregory C. Rutledge *

Department of Chemical Engineering, Massachusetts Institute of Technology, 77 Massachusetts Avenue, Cambridge, MA 02139, USA

Received 14 February 2005; received in revised form 17 May 2005; accepted 24 May 2005
Available online 26 May 2006

Abstract

We describe a method to determine the mechanical and thermodynamic properties of the interface between a polyethylene crystal and melt by united-atom Monte Carlo simulations. In particular, the {201} fold surface is studied in the temperature range 380–450 K. The interface properties are defined by using the concept of a sharp Gibbs dividing surface, which in turn is used to define the interface internal energy and the interface stresses. We find that the internal energy of the interface is of the order 0.3–0.35 J/m^2. The interface stresses are anisotropic for the {201} crystal surface with values of approximately -0.27 and -0.4 J/m^2 for the *xx*- and *yy*-components, respectively. By way of the Herring equation, the surface tension of the fold surface is independent of shear strains in the interface. The temperature and strain derivatives of the interface properties are also measured and discussed in detail. The influence of the interface internal energy and of phase change contributions on the macroscopic heat capacity of the semi-crystalline material is examined.

Keywords: Polymer Interphase; Interfacial stress; Molecular simulation

1. Introduction

Crystallizable polymers are typically not fully crystalline in the solid state. This effect is particularly pronounced when the polymers are considerably longer than the lamella thickness, which leads to chains exiting and re-entering the same or another lamella. Hence, these non-crystalline portions of the chains can never crystallize, even below the melting temperature, due to their connectivity to one or several crystals. A careful characterization of the crystal–melt interface is thus of importance not only for the crystallization process, but also for the properties of the final semi-crystalline material.

Experimentally, the properties of the interface are difficult to measure. When it comes to thermodynamics or mechanical properties, one often has to rely on indirect measurements. For example, the planar stresses in the lamellar fold surface distort the crystal lattice spacings, the distortion being more pronounced for thinner lamellae [1]. By using experimental data on the lattice spacings as a function of lamella thickness in conjunction with data on the mechanical stiffness of the crystal, Cammarata et al. [1–3] were able to draw conclusions about the magnitude of the interface stresses. They found the stresses to be of the order of -0.1 to -0.3 J/m^2 for a {001} surface, depending on the experimental values used. The fact that the interface is actually under pressure can be attributed to the way the polymer chains exit the crystal. First, some of them re-enter the same crystal and the (tight) bending of the chain tries to push both anchor points apart; second, the chains have a higher mobility just above the crystal surface but are constrained by having one end fixed in the crystal. Further indirect measurements of thermodynamic properties include predictions on the surface tension of the fold surface, which in turn enters in theoretical models for experimentally measurable crystallization rates [4,5]. One finds a value of approximately $+0.1$ J/m^2 for the surface tension of polyethylene, i.e., the same order of magnitude as the interface stresses, but with opposite sign. According to Cammarata and Sieradzki [3], for most solids the interface stresses are generally of the same order of magnitude as the surface tension, and can be negative or positive. Interface stresses are believed to be important for the effects of lamellar twisting [6]. In order to result in twisting, the stresses on the opposite fold surfaces of the lamella need to be different. It is argued that such asymmetry may indeed occur if the chains are tilted with respect to the fold surface normal [7,8], such as is the case for a {201} polyethylene surface. Other effects of interface stresses are discussed by Rault [9].

The interlamellar phase has been studied by Monte Carlo molecular simulations previously [10–13]. The structure of the

* Corresponding author. Tel.: +1 617 253 0171; fax: +1 617 258 8992
E-mail address: rutledge@mit.edu (G.C. Rutledge).

0032-3861/$ - see front matter © 2006 Elsevier Ltd. All rights reserved.
doi:10.1016/j.polymer.2005.05.160

loop surface is determined by entropically driven disordering of the chains away from the surface, and enthalpically favored packing of short loops close to the surface. Further studies showed that the {201} crystal surface is energetically favored over other surfaces, in agreement with experimental observations [14]. Structural and in particular the thermodynamic and mechanical properties of the metastable interlamellar phase *as a whole* have been studied extensively for freely rotating chains [15] and for polyethylene [16]. In this paper, we concentrate on the properties of the interface *alone*. We choose to coarse-grain the spatially gradual transition between the crystal and the melt phase into a sharp interface model, namely, using the concept of the Gibbs dividing surface. This definition, as proposed by Gibbs, provides a solid foundation for a detailed discussion of the interface properties. By doing so, one is rewarded with the necessary ingredients, e.g. energy per unit area of the interface and the interface stresses, for a three component model (two bulk phases and interface) on a coarser modeling scale.

Here, we estimate thermodynamic properties and interface stresses based on a united-atom Monte Carlo simulation. As suggested by Fisher, Eby and Cammarata [3], it is important to consider other than tight folds, and to study crystal surfaces other than {001}. We use a Monte Carlo scheme that does not impose constraints on the topology and fold structure of the interface, and we study the commonly observed {201} surface of polyethylene crystals. The manuscript is organized as follows. The simulation technique and the method of interface thermodynamics using the Gibbs dividing surface are described in Section 2, before the results of the simulation are discussed in detail. We conclude with Summary and Discussion.

2. Method

2.1. Simulation technique

2.1.1. Force field

We use the united atom model of Paul et al. [17] for polyethylene, slightly modified as described in our previous work [16], including the torsion angle terms. A Lennard-Jones potential is used to compute the non-bonded CH_2 interactions between all united atom pairs on different chain segments and those separated by four or more bonds in the same chain segment

$$E_{\mathrm{LJ},ij} = 4\varepsilon_{\mathrm{LJ}}\left[\left(\frac{\sigma_{\mathrm{LJ}}}{d_{ij}}\right)^{12} - \left(\frac{\sigma_{\mathrm{LJ}}}{d_{ij}}\right)^{6}\right], \quad \text{with } d_{ij} = |\mathbf{r}_i - \mathbf{r}_j|, \tag{1}$$

with $\varepsilon_{\mathrm{LJ}} = 390.95$ J/mol and $\sigma_{\mathrm{LJ}} = 0.4009$ nm; $\mathbf{r}_i$ and $\mathbf{r}_j$ represent the Cartesian coordinates of sites i and j. The Lennard-Jones interactions are truncated at a cut-off distance $r_c = 2.5\sigma_{\mathrm{LJ}}$. Long range corrections for Lennard-Jones interactions and for virial calculations are included, as discussed by In 't Veld and Rutledge [15]. In addition to these non-bonded interactions, there are three types of bonded interactions included. The bond stretching potential is harmonic in bond length

$$E_{l,i} = \frac{1}{2}k_l(l_i - l_0)^2, \tag{2}$$

where l_i is the length of bond i; the bond stretching constants are $k_l = 376.1$ MJ/mol/nm^2 and $l_0 = 0.1530$ nm. The bond bending potential is harmonic in the cosine of the bond angle

$$E_{\theta,i} = \frac{1}{2}\frac{k_\theta}{\sin^2\theta_0}(\cos\theta_i - \cos\theta_0)^2, \tag{3}$$

where θ_i is the complement of the bond angle constructed by bonds i and $i-1$; the angle bending constants are $k_\theta = 502.1$ kJ/mol and $\theta_0 = 68.0°$. The bond torsion potential, after rearrangement using trigonometric identities, has the form

$$E_{\phi,i} = \sum_{n=0}^{3} k_n \cos^n \phi_i, \tag{4}$$

where ϕ_i is the bond torsion angle constructed by bond pairs $\{i, i-1\}$ and $\{i-1, i-2\}$, namely the angle between the vectors $\Delta\mathbf{r}_i \times \Delta\mathbf{r}_{i-1}$ and $\Delta\mathbf{r}_{i-1} \times \Delta\mathbf{r}_{i-2}$ with $\Delta\mathbf{r}_i \equiv \mathbf{r}_i - \mathbf{r}_{i-1}$. The torsion constants are $k_n \in \{6.498, -16.99, 3.626, 27.11\}$ kJ/mol. The total torsion energy is the sum over all available torsion angles.

2.1.2. Virial calculation of stress

For each of the force field contributions described above, there is a corresponding contribution to the virial. The total instantaneous stress tensor $\boldsymbol{\sigma}$ is then expressed in terms of the virial contributions $\mathbf{W}$ as

$$\boldsymbol{\sigma} = -\frac{1}{V}\left[\sum_{i=1}^{N_{\mathrm{sites}}-1}\sum_{j=i+1}^{N_{\mathrm{sites}}}\mathbf{W}_{\mathrm{LJ},ij} + \sum_{i=1}^{N_l}\mathbf{W}_{l,i} + \sum_{i=1}^{N_\theta}\mathbf{W}_{\theta,i} + \sum_{i=1}^{N_\phi}\mathbf{W}_{\phi,i} + \mathbf{W}_{\mathrm{ideal}}\right], \tag{5}$$

which is the summation over all contributions due to Lennard-Jones interactions, bond lengths, bond angles, and bond torsions. The last contribution is the ideal gas contribution, $\mathbf{W}_{\mathrm{ideal}} = N_{\mathrm{sites}}k_{\mathrm{B}}T$. For the explicit expressions of the other virial contributions, the reader is referred to In 't Veld et al. [15,16].

2.1.3. Simulation setup and sampling

We use a simulation box consisting of a rigid crystal phase and a mobile interlamellar phase as a model for semi-crystalline polyethylene. The interlamellar phase includes both interface and amorphous phase components. The goal of studying the interface between crystal and melt also at temperatures different than the melting temperature requires that one impose certain constraints on the system which hinder it from melting or crystallizing. In order to prevent crystallization at low temperatures, the volume is held constant, while in order to prevent melting at high temperatures the crystal sites are immobile. Rigorously speaking, the interlamellar phase is

metastable under these conditions [18]. In this study we calculate the energy density and the stress tensor components as a function of position. As will become clear below, it is important that both the melt and the crystal phases are at the same stress (e.g. atmospheric) far away from the interface. Since the force field we use has been optimized to describe the melt state, the stresses in the crystal when using experimental lattice parameters are not atmospheric. Therefore, we adjust the lattice parameters in order to use the same force field throughout the entire simulation cell and achieve atmospheric conditions in both the crystal and the melt. For this purpose, we required that the temperature-adjusted configurational stress plus the temperature-dependent ideal gas contribution equal atmospheric pressure for each temperature. The lattice parameters that lead to atmospheric conditions in the crystal for this forcefield are $a(T) = (0.774053 + 0.0000471 \times (T - 400))$ nm, $b(T) = (0.445817 + 0.0000261 \times (T - 400))$ nm, and $c(T) = (0.252748 + 0.0000014 \times (T - 400))$ nm, where T is the temperature in units of K. As confirmed a posteriori, these relations are sufficient to ensure atmospheric conditions within 6 MPa in the crystal (which is negligible with respect to the local pressures in the interface) over the entire temperature range considered here. More realistic thermal expansion behavior could be determined a priori through a separate crystal phase simulation that samples the full anharmonicity of the vibrational modes in the crystal lattice with interaction forces suitable for the crystalline phase, but this was not done here. Using the lattice parameters given above, the orthorhombic unit cell attains hexagonal symmetry in the *ab*-plane, as is typical for united atom models of polyethylene. We choose to study the {201} crystal surface, which is found experimentally to be the most common fold surface for polyethylene [14]. A schematic diagram of the simulation box is shown in Fig. 1. The size of the simulation cell corresponds to $3a/\cos(\alpha_{\text{tilt}}) \simeq 2.77$ nm with tilt angle $\alpha_{\text{tilt}} = \arctan(2c/a)$ and $6b \simeq 2.67$ nm in the x- and y-directions, respectively. In the z-direction normal to the crystal surface, we use a crystal of 2.62 nm thickness on both ends of the simulation cell and approximately 7.22 nm of mobile interlamellar phase. The pressure in the melt phase far away from the interface also is adjusted to have atmospheric conditions by changing the z-extension of the interlamellar phase. The values for the densities of the crystal and melt used in the simulations are reported in Fig. 2. We point out that the chosen intercrystalline phase dimension is realistic for a semi-crystalline material formed at large undercooling [19]. The mobile interlamellar phase consists of $N_{\text{sites}} = 1944$ (at $T = 380$ K) to $N_{\text{sites}} = 1960$ (at $T = 450$ K) united atoms, which are grouped into 18 tail molecules and 27 loop and bridge molecules. Following the simplified chain length statistics described elsewhere [18], crystal stems of 100 united atoms (corresponding to a separation of approximately 10.5 nm between the two surfaces of a {201} crystal) in conjunction with the interlamellar material simulated here would correspond to a polyethylene of molecular weight 9630 g/mol and 60% crystallinity. Phase space is sampled in Monte Carlo fashion by topology altering (end-reptation and end-bridging) and displacement (end-rotation, rebridging, and single-site displacement) moves, as explained in our previous paper [15]. In addition, we facilitate a more efficient sampling of phase space at lower temperatures by applying parallel tempering. Our parallel tempering scheme uses a temperature profile as prescribed by Kofke [20] to ensure equal swapping probability between neighboring temperatures (an acceptance of 35% is observed). The temperature profile is given by $T \in \{380.6, 391.4, 402.4, 413.8, 425.6, 437.6, 450\}$ K. We note that the simulation boxes participating in the same parallel tempering simulation all have the same volume, although they have different temperatures. As a consequence, in a single parallel tempering simulation, atmospheric conditions are satisfied in the bulk phases far away from the crystal surface only for one specific temperature. Hence, in order to get interface properties with respect to bulk phases at atmospheric conditions at different temperatures, we perform many parallel-tempering simulations.

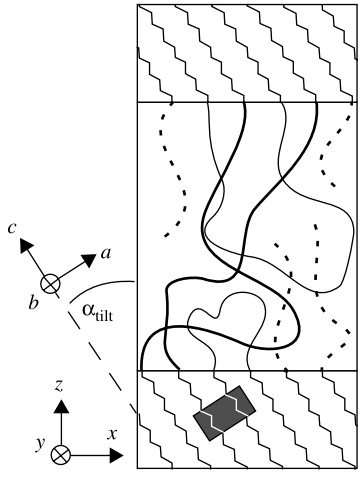

Fig. 1. Schematic diagram of the simulation box, showing the two crystalline lamellae and the interlamellar phase in between, which consists of loops (thin solid lines), bridge chains (thick solid lines), and tails (dashed lines). The polyethylene unit cell (grey box) with coordinate axes (a,b,c) is tilted by an angle α_{tilt} with respect to the surface normal and the coordinate system (x,y,z).

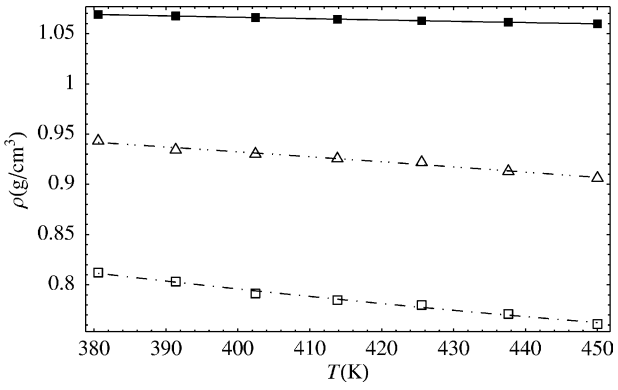

Fig. 2. Crystal (■), melt (□), and volume averaged (△) mass densities used in the simulations as a function of temperature.

2.1.4. Initial configuration

A {201}-oriented crystal of 36 chains with 120 united atom CH_2 sites in an orthorhombic box serves as the starting point for the initial structure. We immobilize the first and last 25 sites of each chain, after which 27 chains are selected at random to serve as bridge molecules. The remaining nine chains are split in half to serve as tails, after which sites are then deleted from the mobile ends to satisfy approximately the density requirement for the interlamellar phase for atmospheric conditions. The density of the interlamellar phase then is fine-tuned by affinely deforming the mobile region. Once created, randomization of this configuration takes place at $T=10{,}000$ K for 1000 cycles to ensure a fully amorphous interlamellar phase. Here, a cycle is defined as N_{sites} Monte Carlo moves, with N_{sites} being the total number of sites in the simulation cell, including the immobile crystal sites. These randomized configurations are quenched to $T=5000$ K for 10,000 cycles, then to $T=2000$ K for 10,000 cycles, then to $T=1000$ K for 10,000 cycles, and finally to the desired temperatures {380.6, 391.4, 402.4, 413.8, 425.6, 437.6, 450} K, and equilibrated for 25,000 cycles before any measurements are taken. Decay studies of the energy autocorrelation function confirm equilibration in less than 25,000 cycles.

Deformation is treated according to respective regions. United atom sites in crystalline or immobile chain segments are considered intra-molecularly rigid and thus, when deformed, are displaced with respect to a common reference or anchor point. This anchor point is defined as the intersection of the segment's molecular axis with the nearest simulation box face in the z-direction (at $z=\pm(1/2)L_z$). Like the interlamellar phase or mobile united atom sites, anchor points are deformed in regular affine fashion, regardless of the deformation direction. This particular approach assures treatment of both top and bottom crystal phase as one continuous phase. Once deformed, a configuration is equilibrated for 25,000 cycles.

2.1.5. Profiles of energy density and stresses

Measuring the energy density and the components of the stress tensor as a function of the z-direction (normal to the crystal surface) is an essential ingredient for the calculation of the interface properties. These profiles are measured with a resolution of $\Delta z=0.035$ nm. In order to calculate the local energy and stress components in each bin, one considers all types of interactions (Lennard-Jones, bond length, bending angle, torsion) and apportions the corresponding energy and stress contribution equally to each of the particles involved. For clarification, we illustrate the procedure on the example of the torsion interaction, which involves the relative positions of four particles. Since the positions of all four particles are equally important for the value of the torsion energy, we assign a quarter of the energy and a quarter of the stress components to each of the four particles. In doing so, we make sure that all contributions are counted exactly once. In the course of the Monte Carlo simulation, we calculate for each bin the average energy and the average stresses per particle. This is then multiplied by the local number density, in order to obtain the final energy density and stress component profiles. The long range correction for the Lennard-Jones interaction has been accounted for in the profiles of both the energy and the stresses.

2.2. Interface thermodynamics

The procedure to obtain the thermodynamic and mechanical properties of the interface is best described by considering a specific example, here the polyethylene crystal–melt interface. A more detailed and complete description can be found elsewhere [21–23]. The mass density profile versus surface normal direction, z, shown in Fig. 3 is obtained by considering each united atom as a sphere of Lennard-Jones diameter σ_{LJ}. For each united atom, its mass is split up and distributed over all bins in the z-direction which are closer than $\sigma_{\text{LJ}}/2$ to the united atom center position, according to the sphere volume falling into each bin. The mass density transitions gradually between the crystal density (left side in Fig. 3) to the melt density (right side in Fig. 3). In coarse-graining, we approximate this gradual transition as a step function, where everything to the left of the step is identical to the crystal far away from the interface, and everything to the right is identical to the melt far away from the interface. The sharp interface is known as the Gibbs dividing surface [21,22]. Here we adopt the common definition that the Gibbs dividing surface is chosen such that the integral of the true mass density profile equals the integral of the step function, which amounts to the conservation of mass. Hence, the interface mass density (kg/m^2)

$$\rho_{\text{int}} := \int_{-\infty}^{\infty} (\rho(z) - \rho^{\text{step}}(z|z_{\text{div}}))\mathrm{d}z = 0 \tag{6}$$

vanishes for this particular position of the dividing surface, z_{div}. Here z describes the spatial variable perpendicular to the interface. The fact that the interface is massless has important ramifications for the interface thermodynamics [22], e.g. the chemical potential of the interface vanishes. In order to define the interface energy, one next replaces the true energy profile as shown in Fig. 4 (open symbols) by a step function, where the step is located at the position determined previously from the mass density profile, z_{div}. In general, the energy of the total system based on the step profile and on the true profile do not

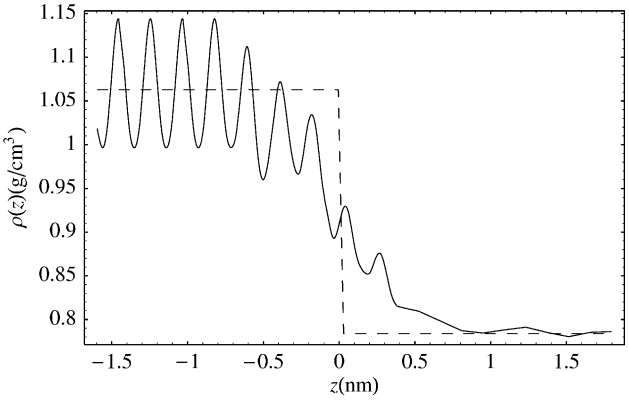

Fig. 3. Profile of mass density. Dashed line shows the profile after the sharp-interface approximation, with the Gibbs dividing surface located at $z_{\text{div}}=0$.

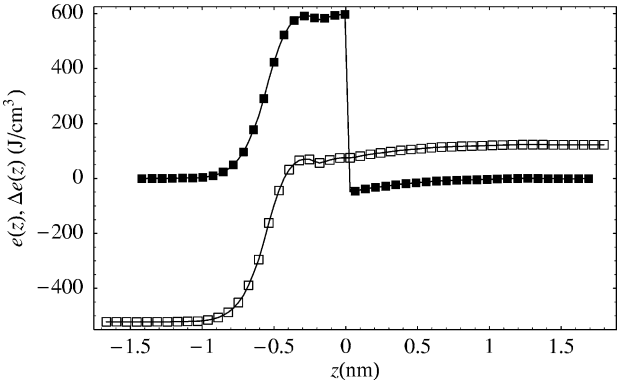

Fig. 4. Profile of energy density: simulated (□), and after subtracting the bulk contributions on the crystal side ($z<0$) and the melt side ($z>0$) (■).

coincide, the difference then being defined as the interface (excess) energy, e_{int}, in order to conserve energy

$$e_{\text{int}} := \int_{-\infty}^{\infty} (e(z) - e^{\text{step}}(z|z_{\text{div}}))\mathrm{d}z \neq 0. \tag{7}$$

In Fig. 4, the integral of the curve with the solid symbols amounts to the internal energy of the interface. With the two definitions (6) and (7) one ensures that the total mass and internal energy based on the step profile representation, including the interface (excess) contributions, equal the values obtained from the true profile representation.

The interface stresses are defined as follows. The stress tensor components can be determined at various positions along the direction of the surface normal (see Fig. 5), $\sigma_{\alpha\beta}(z)$. The interface stresses, $\pi_{\alpha\beta}$, are then defined by [21]

$$\pi_{\alpha\beta} := \int_{-\infty}^{\infty} (\sigma_{\alpha\beta}(z) - \sigma_{\alpha\beta}^{\text{step}}(z|z_{\text{div}}))\mathrm{d}z \neq 0 \quad (\alpha, \beta = x, y), \tag{8}$$

where $\sigma_{\alpha\beta}^{\text{step}}(z|z_{\text{div}})$ defines the step function with step located at z_{div} and where the values at either side of the step correspond to the bulk stress value far away from the interface. Eq. (8) clearly shows that only the contributions due to the presence of the interface are of interest, and the bulk contributions are subtracted by using the Gibbs dividing surface. This is also beneficial with respect to assuming fixed, immobile crystal

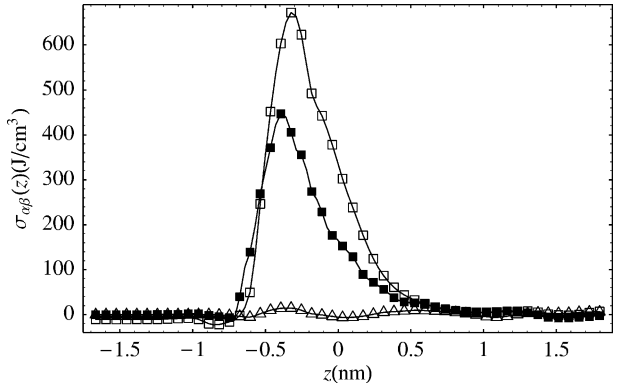

Fig. 5. Profile of stress tensor: $\sigma_{xx}(z)$ (■), $\sigma_{yy}(z)$ (□), and $\sigma_{xy}(z)$ (△).

atoms. The response of the crystal to a change in temperature is captured only approximately by adjusting the crystal structure to the temperatures of interest. However, small errors in the bulk crystal stresses due to e.g. a small imposed strain do not contribute to the interface stresses according to (8). Similarily, small errors in the bulk energy densities are unimportant for the interface energy as defined in Eq. (7). In quiescent conditions and for a planar interface, both phases are at atmospheric conditions far away from the interface, by construction.

It is important to note that the interface stresses are different from the surface tension γ, i.e. from the Helmholtz free energy per unit area, if at least one of the two joining phases is solid [24]. Both quantities are connected in a non-trivial way through the Herring equation [3,25]

$$\pi_{\alpha\beta} = \gamma\delta_{\alpha\beta} + \frac{\partial\gamma}{\partial\epsilon_{\alpha\beta}}, \tag{9}$$

where $\delta_{\alpha\beta}$ denotes the identity matrix. For interfaces in which at least one of the two phases is not fluid, the surface tension depends on the strain in the interface, $\epsilon_{\alpha\beta}$ ($\alpha,\beta = x,y$), in which case the second term in Eq. (9) becomes important. The experimental values reported in Section 1 show that the strain dependence of the surface tension can be so significant that the interface stresses and the scalar surface tension are of opposite sign. While the surface tension measures the reversible work per unit area involved in forming a surface, which exposes new molecules, the interface stresses capture the mechanical response upon deformation of the interface [23].

3. Results and discussion

3.1. Position of the Gibbs dividing surface

The first ingredient in the measurement of the interface internal energy and of the interface stresses is the position of the Gibbs dividing surface. In Fig. 6, the location of the dividing surface determined from the Monte Carlo simulations is reported for a range of temperatures. Because the mass density profiles vary smoothly between the discrete points in

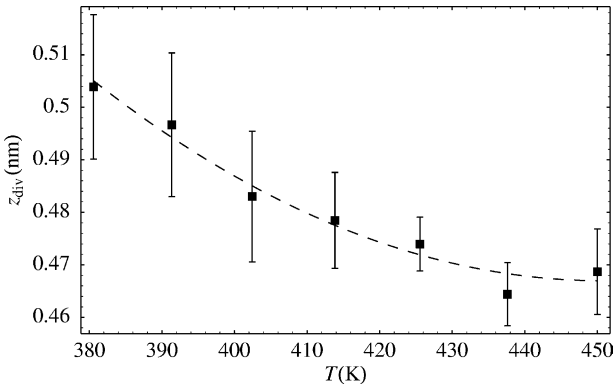

Fig. 6. Position of the Gibbs dividing surface, plotted versus temperature at atmospheric bulk stresses in the adjoining crystal and melt phases. The error bars (as also for Figs. 8 and 11) are calculated by splitting the entire Monte Carlo simulation in 10 blocks. The ten statistically independent block averages are then used to determine the error associated with the total average.

the z-direction (separated by the resolution $\Delta z = 0.035$ nm) we may use interpolation to determine the position of the Gibbs dividing surface more accurately. The position of this surface is measured with respect to the real crystal surface, which is defined midway between the top layer of united atoms in the crystal and the first layer of mobile atoms. For all values reported in Fig. 6, the bulk phases are at atmospheric conditions far away from the interface at the corresponding temperature. Thus, the geometry of the simulation cell varies from temperature to temperature. The results show that the Gibbs dividing surface moves closer to the real crystal surface at the higher temperatures. The thickness of the interface is approximately equal to $2z_{\mathrm{div}}$, from which we can infer that this thickness also decreases for the higher temperatures, in accord with previous results [15,16]. At higher temperatures, melt entropy becomes more important, and the energetically dominated persistence along the chain backbone weakens, resulting in a sharper crystal–melt transition.

Let us now consider the temperature derivative of the position of the dividing surface. The pressure in the bulk phases obviously affects the position of the dividing surface, z_{div}. In more general terms, this means that the description of interface properties must take into account not only the temperature T and the strain in the interface plane $\epsilon_{\alpha\beta}$ ($\alpha,\beta \in \{x,y\}$), but also the pressures in the bulk of the crystal and the melt need to be considered. This has ramifications for the temperature derivative of the position of the dividing surface. While the slope in Fig. 6 is a derivative at constant bulk pressures, $(\partial z_{\mathrm{div}}/\partial T)|_{\epsilon_{\alpha\beta},p_{\mathrm{c}},p_{\mathrm{m}}}$, we wish to calculate the temperature derivative also when keeping the total volume V of the system constant, $(\partial z_{\mathrm{div}}/\partial T)|_{\epsilon_{\alpha\beta},V}$. The values for the latter derivative are reported in Fig. 7. They (and also the data shown in Figs. 9 and 12) are obtained by fitting a linear function through measurements at three successive temperatures of a single parallel tempering simulation, where for the middle temperature the geometry of the simulation cell results in atmospheric conditions in both crystal and melt far away from the interface. While the temperature derivative at constant bulk stresses as determined from Fig. 6 goes from approximately -9×10^{-4} nm/K below $T = 400$ K to zero within error bars above $T = 430$ K, the corresponding values for the constant volume temperature derivatives show the same trend but are larger by a factor of approximately 5. Keeping the volume constant during a temperature increase results in an increased pressure in the melt phase, which in turn further compresses the interface. Because this effect is absent when maintaining bulk pressures at atmospheric conditions, the slope estimated on the basis of Fig. 6 is smaller than the values shown in Fig. 7.

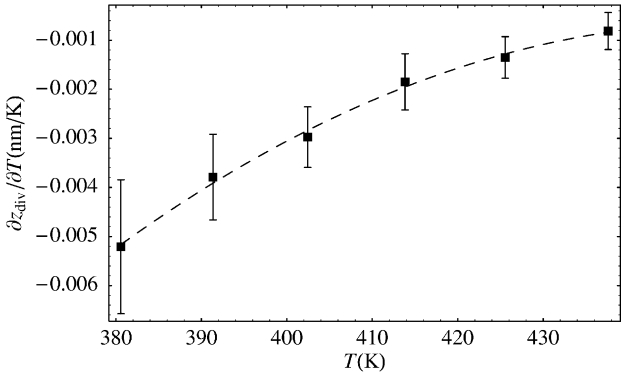

Fig. 7. Temperature dependence of the position of the Gibbs dividing surface at constant interface strain $\epsilon_{\alpha\beta}$ and constant system volume V. Each error bar is calculated by propagating the errors from the three data points at successive temperatures to the slope of the linear fit function.

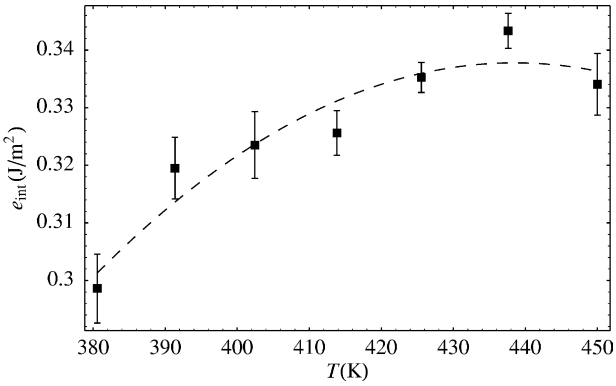

Fig. 8. Interface internal energy, plotted versus temperature at atmospheric bulk stresses in the adjoining crystal and melt phases.

3.2. Internal energy of the interface

The internal energy of the interface is determined from energy density profiles as measured in the Monte Carlo simulations. We then use the procedure described by Eq. (7) with the values for the position of the Gibbs dividing surface z_{div} reported in Section 3.1. The corresponding results are shown in Fig. 8. We see that the interface internal energy steadily increases with increasing temperature up to the melting temperature ($T_{\mathrm{m}} \simeq 410$ K), and remains approximately constant above. The energy values in Fig. 8 are significantly higher than the values calculated previously (0.07 J/m^2) [13], where torsional energy was neglected and the experimental lattice parameters (instead of optimized) were used. In contrast to experimental values for the Helmholtz free energy per unit area (i.e. surface tension) of approximately 0.1 J/m^2 for the fold surface [4,5], the interface internal energies reported here do not include entropic contributions. From a comparison of the experimental data with our simulation results one can estimate that the entropic contribution is given by $Ts_{\mathrm{int}} \simeq 0.2$ J/m^2.

The temperature derivative of a thermodynamic property depends on the variables that are held constant. Different material behavior can be observed when keeping either bulk pressure or total volume constant. Similar to the discussion about the Gibbs dividing surface, we now consider the temperature derivative of the interface internal energy at constant interface strain $\epsilon_{\alpha\beta}$ and constant system volume V. The corresponding values, which are calculated as described in Section 3.1, are reported in Fig. 9. In contrast to a positive slope at constant bulk stresses (Fig. 8), the temperature derivative at constant volume is negative below the melting temperature,

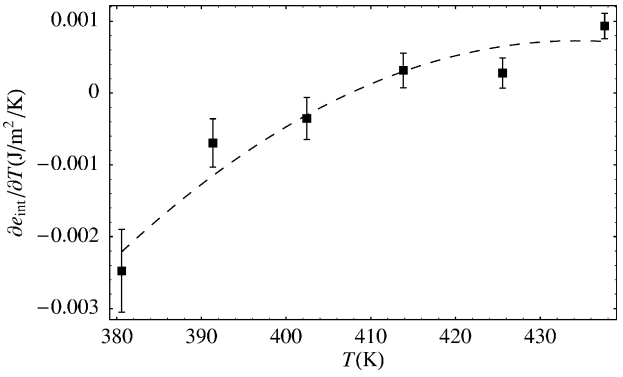

Fig. 9. Temperature dependence of the interface internal energy at constant interface strain $\epsilon_{\alpha\beta}$ and constant system volume V.

and is approximately zero above. The different sign of the slope at low temperatures can be explained as follows. Inspection of the energy profile with respect to the step function, $(e(z)-e^{\rm step}(z|z_{\rm div}))$, shows that its value on the crystal side close to the dividing surface is higher for higher temperatures, while the melt side is relatively unchanged. This would result in a higher interface internal energy at higher temperatures, *if* the position of the dividing surface was constant. However, we know that the dividing surface moves closer to the crystal at the higher temperature. The sensitivity with which this happens decides if the total interface energy change is positive or negative. Temperature changes at constant volume result in a much larger change of interface position than when considering constant bulk pressures (for reasons given in Section 3.1). Hence, we conclude that the interface energy change with respect to temperature must be smaller at constant volume (and may even go negative as the data in Fig. 9 show) than at constant bulk pressures. The difference in the temperature dependence of interface location, $\partial z_{\rm div}/\partial T$, at constant volume and at constant pressure obscures any simple relation between the temperature derivatives of interfacial energy such as exists for isochoric and isobaric heat capacities of bulk phases.

In analogy to the heat capacity at constant volume of bulk materials, one may call either $(\partial e_{\rm int}/\partial T)|_{\epsilon_{\alpha\beta},p_{\rm c},p_{\rm m}}$ or $(\partial e_{\rm int}/\partial T)|_{\epsilon_{\alpha\beta},V}$ a 'heat capacity at constant surface area' of the interface. However, we did not choose that nomenclature on purpose in view of the fact that $e_{\rm int}$ itself is an excess property. The behavior of that excess property upon changing temperature does describe the ability to store energy, but it is strongly interwoven with the thermodynamic behavior of the two adjoining bulk phases. We now discuss how the temperature derivative of the interface energy at constant volume relates to the heat capacity C_V of the entire simulation cell, which is shown in Fig. 10, in accord with previous results [15,16]. The position of the Gibbs dividing surface changes with respect to temperature, as discussed above. In terms of the coarse, discretized three component model this means that the crystal either grows or shrinks. When considering the total internal energy of the system, $E_{\rm t}(T)$, it becomes clear that the temperature derivative, $\partial E_{\rm t}(T)/\partial T|_V$, includes also phase transformation effects. To illustrate this one can write $E_{\rm t}(T)$ in the form

$$E_{\rm t}(T) = A\left[e_{\rm c}(T)\bar{z}_{\rm div}(T) + e_{\rm m}(T)(L-\bar{z}_{\rm div}(T)) + e_{\rm int}(T)\right], \quad (10)$$

with sample cross section A, internal energy densities of the crystal and melt, $e_{\rm c}$ and $e_{\rm m}$, respectively, the length of the sample L, and the position of the Gibbs dividing surface with respect to the crystal end of the simulation cell, $\bar{z}_{\rm div}$. Eq. 10 is equivalent to the previous definition of the interface energy, Eq. (7). The temperature derivative of that expression consists of bulk terms, the temperature change of the interface energy, and a phase change contribution proportional to $\partial\bar{z}_{\rm div}/\partial T = \partial z_{\rm div}/\partial T$

$$\frac{1}{A}\frac{\partial E_{\rm t}(T)}{\partial T} = \frac{\partial e_{\rm c}(T)}{\partial T}\bar{z}_{\rm div}(T) + \frac{\partial e_{\rm m}(T)}{\partial T}[L-\bar{z}_{\rm div}(T)] + [e_{\rm c}(T)-e_{\rm m}(T)]\left[\frac{\partial\bar{z}_{\rm div}(T)}{\partial T}\right] + \frac{\partial e_{\rm int}(T)}{\partial T}, \quad (11)$$

where all derivatives are taken at constant volume of the simulation cell, V. Two points are important for interpretation of the total 'heat capacity' $C_V \equiv (\partial E_{\rm t}/\partial T)|_V$ as reported in Fig. 10. First, the quantity $\partial e_{\rm c}(T)/\partial T$ is the heat capacity of the crystal phase at constant volume, because the crystal cannot expand. For the liquid phase, the term $\partial e_{\rm m}(T)/\partial T$ is not a heat capacity because neither the pressure of the melt phase alone nor the mass density of the melt phase alone are constant (as confirmed by our simulations) when changing the temperature and holding the total volume of melt plus interface constant. Second, and more importantly, the quantity $e_{\rm int}(T)$ according to Eq. (10) for each given temperature is defined with respect to a temperature-dependent dividing surface position. Therefore, the temperature derivatives $\partial e_{\rm int}/\partial T$ reported in Fig. 9 are taken with respect to a frame of reference that moves with the Gibbs dividing surface, and hence they do not include any phase transformation contributions. The latter are explicitly accounted for in Eq. (11) by a separate term, which accounts for a latent heat-type contribution to the 'apparent' heat capacity of the interlamellar region. In our simulations we observe that the last two terms of Eq. (11) are comparable in magnitude. While at $T=380$ K one finds $[e_{\rm c}(T)-e_{\rm m}(T)]\bar{z}_{\rm div}$

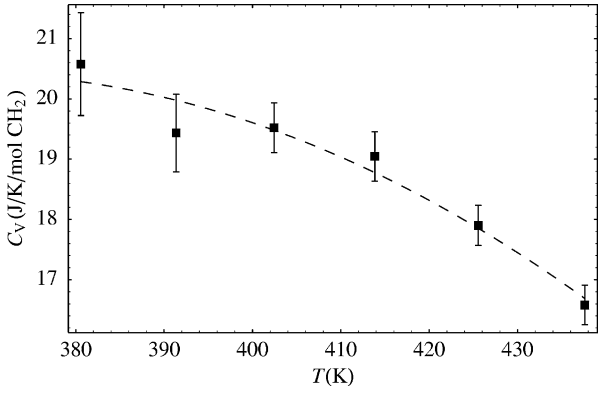

Fig. 10. Heat capacity of the entire simulation cell at constant interface strain $\epsilon_{\alpha\beta}$ and constant system volume V, including crystal, melt and interface contributions.

$\simeq 0.003$ J/m^2/K and $\dot{e}_{\rm int} \simeq -0.0025$ J/m^2/K with opposite sign, one has $[e_{\rm c}(T) - e_{\rm m}(T)]\dot{\bar{z}}_{\rm div} \simeq 0.0005$ J/m^2/K and $\dot{e}_{\rm int} \simeq 0.0008$ J/m^2/K with the same sign for $T = 437$ K. The first two contributions in Eq. (11) obviously depend on the absolute thickness of the crystal and of the interlamellar region, respectively. In the simulations performed here one finds for the melt contribution $\dot{e}_{\rm m}(L - \bar{z}_{\rm div}) \simeq 0.007$ J/m^2/K at $T = 380$ K and 0.006 J/m^2/K at $T = 437$ K, while the crystal contribution is vanishingly small. In summary, the temperature derivative of the total internal energy of the semi-crystalline system is complicated by the temperature-dependent location of the Gibbs dividing surface, which gives rise to a latent heat-type contribution, and in particular the contribution of the interface internal energy needs to be accounted for.

3.3. Interface stresses

The interface stresses are calculated according to Eq. (8) using the spatially resolved stresses profiles across the interface (see e.g. Fig. 5). The corresponding values for the interface stresses are reported in Fig. 11 for the bulk crystal and melt being at atmospheric conditions. The off-diagonal interface stress π_{xy} is zero within errors, while the diagonal stresses are clearly non-zero.

Firstly, it is important to note that the interface stresses are negative, meaning that the stresses try to expand the interface. As explained in Section 1, this is conceivable because the chains are congested as they exit the crystal, and (short) folds also preferentially try to increase the distance between anchor points. Our results agree in sign and magnitude with the results reported by Cammarata, Eby and Fisher [1–3], who took into account experimental data and used a crystal of orthorhombic symmetry. In that respect, we can say that our results relate to experimental reports reasonably well, despite the hexagonal symmetry of the united atom crystal used here. It is important to note, however, that Cammarata et al. [1–3] studied the {001} crystal surface, whereas we focus on the {201} surface, which precludes a direct comparison of the actual values. According to Rault [9], the interface stresses are high (and anisotropic) in the presence of short folds. In the absence of short folds, the interface stresses are expected to be low compared to the value of the surface tension. Our current simulations show that the average loop consists of $\langle L_{\rm loop} \rangle \simeq 35.3 - 0.09 \times (T[\mathrm{K}] - 400)$ mobile united atoms. Since the loop length distributions are approximately exponential [13], about two thirds of all chains are shorter than the average. In that respect, our simulations correspond to the case of rather short (but not tight[1]) folds, which according to Rault is in agreement with the observed large absolute value of the interface stresses ($|\pi_{xx}|, |\pi_{yy}| > \gamma$) and their anisotropy, $\pi_{xx} \neq \pi_{yy}$. This anisotropy is a fingerprint of the broken symmetry of the {201} surface, which has chains exiting tilted away from the surface normal direction (z-direction) in the xz-plane. Unequal diagonal components of the interface stresses were also reported for the {001} surface by Cammarata, Eby and Fisher [1–3]. In their case, it is due to the orthorhombic symmetry of the underlying crystal.

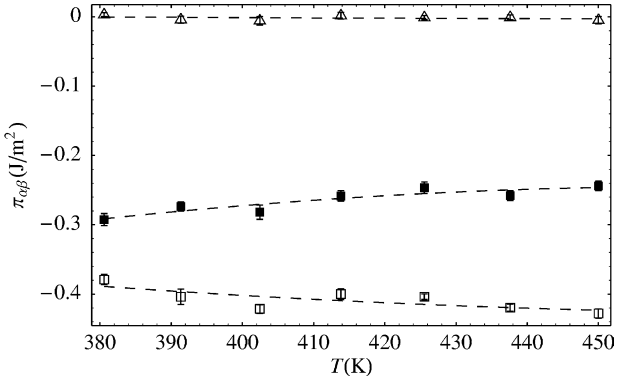

Fig. 11. Interface stresses, plotted versus temperature at atmospheric bulk stresses in the adjoining crystal and melt phases: π_{xx} (■), π_{yy} (□), and π_{xy} (△).

Secondly, the fact that the off-diagonal interface stress vanishes is particularly interesting. By way of the Herring equation (9) we find that the surface tension does not depend on shear deformations of the interface, i.e. $\partial\gamma/\partial\epsilon_{xy} = 0$ at this state of zero deformation, $\epsilon_{\alpha\beta} = 0$ ($\alpha,\beta \in \{x,y\}$). It is only for the off-diagonal parts of the interface stresses that one can draw conclusions about the strain dependence of the surface tension, because for the diagonal parts both contributions in the Herring equation (9) contribute to the interface stress.

In the Monte Carlo simulation, the stress tensor profiles $\sigma_{\alpha\beta}(z)$ are calculated not only for the in-plane components (i.e. for $\alpha,\beta \in \{x,y\}$), but also for all other components. In mechanical equilibrium, one ideally has $\sigma_{xz}(z) = \sigma_{yz}(z) \equiv 0$, and $\sigma_{zz}(z)$ must be constant. As discussed in Section 1, the crystal sites are fixed in our simulation in order to prevent melting of the crystal above the melting temperature. However, one expects that this introduces artificial stresses in the interface (but not so in the crystal away from the interface, because its structure is adjusted accordingly). As a useful measure for the magnitude of the artificial stresses, we use the definition given by Eq. (8) also for these out-of plane stresses. One finds that $|\pi_{xz}| \lesssim 0.05$ J/m^2, $|\pi_{yz}| \lesssim 0.01$ J/m^2, and $|\pi_{zz}| \lesssim 0.05$ J/m^2. Hence, the stress integrals involving the z-direction are 20% or less in magnitude compared to π_{xx}, and even smaller when compared to π_{yy}. Nevertheless, they are significant, and the reason is that the chains exit the crystal tilted with respect to the surface normal, and try to stand up parallel to the surface normal in order to have more space. However, because they are connected to the crystal, the persistence along the backbone hinders them considerably from doing so, in particular because even the top crystal layers are held in place rigidly. Hence, we believe that the stresses π_{xz} and π_{zz} are a signature of the tilted chains and of their persistence along the backbone.

The temperature derivatives of the interface stresses at constant interface strain and constant system volume are shown in Fig. 12. They are analogous to the thermal stress coefficient

[1] The minimum fold length observed in the simulation is seven united atoms. Therefore, the surface studied here is clearly distinct from a tight fold surface.

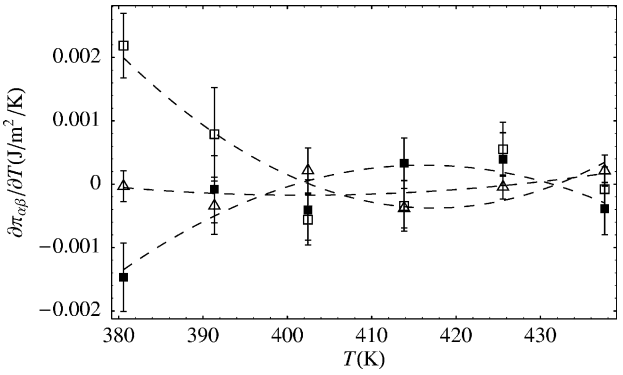

Fig. 12. Temperature dependence of the interface stresses at constant interface strain $\epsilon_{\alpha\beta}$ and constant system volume V : $(\partial\pi_{xx}/\partial T)_{\epsilon_{\alpha\beta},V}$ (■), $(\partial\pi_{yy}/\partial T)_{\epsilon_{\alpha\beta},V}$ (□), and $(\partial\pi_{xy}/\partial T)_{\epsilon_{\alpha\beta},V}$ (△).

in bulk thermodynamics, $(1/p)(\partial p(T,V)/\partial T)|_V$. We find that the interface stresses have a negligible temperature dependence above the melting temperature, within error bars. However, at low temperatures, a 10 K temperature change results in a stress change of the order of 5% for both π_{xx} and π_{yy}, when comparing to the data reported in Fig. 11. Furthermore, one should note that at low temperatures the temperature derivatives at constant bulk pressures or at constant system volume, respectively, have opposite sign, similarly to the effect for the interface internal energy (cf. Section 3.2). This highlights again that it is important to keep track of the control variables. Davis et al. [26] determined experimentally the change in lattice spacing due to interface stresses as a function of temperature. According to their results the change in the lattice parameters a and b have opposite sign and a strong temperature dependence of the interface stresses is inferred. Unfortunately, however, their results cannot be compared to the simulations presented here, because the simulated crystal has different lattice spacing than the experimental system. It also has a different crystal symmetry (hexagonal, in contrast to orthorhombic), and hence also the mechanical behavior is significantly different. In view of possible future studies of the polyethylene interface we note that the temperature derivative of the interface stresses at constant strain are essential ingredients for the calculation of the thermal expansion coefficients [27] $\alpha_{ij}|_\pi = \sum s_{ijkl}(\partial\pi_{kl}/\partial T)|_\epsilon$ with the fourth rank stiffness tensor $s_{ijkl} = (\partial\epsilon_{ij}/\partial\pi_{kl})|_T$ of the interface.

3.4. Effect of interface strain

The strain dependence of the interface internal energy and interface stresses is of interest because it reveals additional information about the system. For example, the strain derivatives of the interface stresses lead to the fourth rank stiffness tensor. Since the interface in our case is planar and oriented in the xy-plane, we only consider deformations in the xy-plane. The simulation cell consists of two bulk phases and the interface. A deformation can be imposed in different ways [3]. Considering a tension along the x-direction, first, equal stress can be applied in this direction to both crystal and melt. However, since these two phases have different stiffnesses, they are deformed to different strains. Consequently, a proper definition of how to deform the interface becomes cumbersome. Another method consists in deforming all phases (i.e. the entire simulation cell) with the same strain. In that case the planar strain in the interface, $\epsilon_{\alpha\beta}$, is defined unambiguously.

Let us first discuss the change of the Gibbs dividing surface position when imposing a strain in the x- or y-direction. Consider a situation as depicted in Fig. 3, with crystal mass density $\rho_c := \lim_{z\to -L/2}\rho(z)$ and melt mass density $\rho_m := \lim_{z\to L/2}\rho(z)$ for a sufficiently large value of L. Without loss of generality one can write $\rho(z) = \rho_c(1 - f(z))$, with $f(z)$ a function that vanishes in the crystal and equals $1-(\rho_m/\rho_c)$ in the melt. The definition of the position of the Gibbs dividing surface, Eq. (6), can then be rephrased into

$$z_{\text{div}} = \frac{L}{2} - \frac{1}{1-\rho_m/\rho_c}\int_{-L/2}^{L/2} f(z)\mathrm{d}z. \tag{12}$$

The change of z_{div} with respect to strain can now be discussed more easily. One can show that the integral in Eq. (12) is invariant with respect to strains in the x- or y-direction. In particular it is positive. One then finds that $(\partial z_{\text{div}}/\partial\epsilon_{\alpha\alpha})|_T$ and $(\partial(\rho_m/\rho_c)/\partial\epsilon_{\alpha\alpha})|_T$ ($\alpha\in\{x,y\}$) are of opposite sign. Since the crystal has a lower compressibility than the melt, one can argue that the material between the bulk crystal and the bulk melt also has a lower compressibility than the melt. If the entire simulation cell is under strain, the percentage decrease of the density is higher in the melt than in the crystal, whereby one has $(\partial(\rho_m/\rho_c)/\partial\epsilon_{\alpha\alpha})|_T < 0$. Hence, the transition region expands upon expansion of the entire system by virtue of Eq. (12), and the position of the Gibbs dividing surface is pushed away from the real crystal surface. This is clearly against the intuition that the chains that exit the crystal have more space available in the xy-plane if their anchor points on the crystal surface are moved apart, and hence they would relax over a shorter distance from the crystalline conformation to a random conformation. The data in Fig. 13 show that under strain the melt density indeed decreases more than the crystal density, and therefore the distance between the crystal surface and the Gibbs dividing

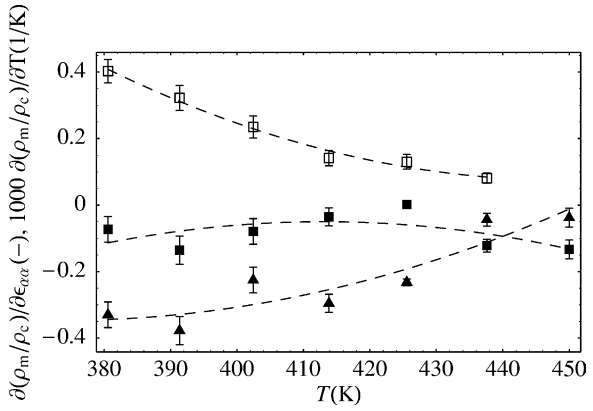

Fig. 13. Strain dependence of the ratio of bulk mass densities at constant temperature: $(\partial(\rho_m/\rho_c)/\partial\epsilon_{xx})|_T$ (■) and $(\partial(\rho_m/\rho_c)/\partial\epsilon_{yy})|_T$ (▲). For comparison, the temperature dependence at constant interface strain $\epsilon_{\alpha\beta}$ and constant system volume V is also shown, $(\partial(\rho_m/\rho_c)/\partial T)|_{\epsilon_{\alpha\beta},V}$ (□).

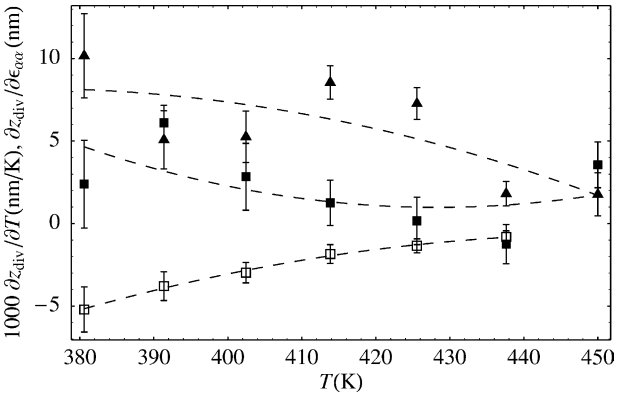

Fig. 14. Strain dependence of the position of the Gibbs dividing surface at constant temperature: $(\partial z_{\rm div}/\partial \epsilon_{xx})|_T$ (■) and $(\partial z_{\rm div}/\partial \epsilon_{yy})|_T$ (▲). For comparison, the temperature dependence at constant interface strain $\epsilon_{\alpha\beta}$ and constant system volume V is also shown, $(\partial z_{\rm div}/\partial T)|_{\epsilon_{\alpha\beta},V}$ (□).

surface increases, as shown in Fig. 14. We note that Eq. (12) also holds for the case of isochoric temperature changes. Therefore, also for the temperature derivative at constant interface strain and system volume, the quantities $(\partial z_{\rm div}/\partial T)|_{\epsilon_{\alpha\beta},V}$ and $(\partial(\rho_{\rm m}/\rho_{\rm c})/\partial T)|_{\epsilon_{\alpha\beta},V}$ must be of opposite sign, which is confirmed by the data shown in Figs. 13 and 14.

The strain derivatives of the position of the Gibbs dividing surface are rather irregular as a function of temperature in comparison to the temperature derivatives (see Fig. 14), which is an indication of the size of the true error on these strain derivatives. The error bars reported in Fig. 14 are based on block averages as discussed previously. However, due to the finite duration of the simulation, the profiles do not get completely flat in the bulk of the melt. Eq. (12) shows how, e.g. errors in ρ_m lead to errors in $z_{\rm dim}$. We envisage the following origin for such additional errors which strongly influence the strain derivatives of $z_{\rm div}$, and also of $e_{\rm int}$ and $\pi_{\alpha\beta}$. All interface properties depend strongly on the position $z_{\rm div}$ as well as on an accurate determination of the bulk properties from the profiles. Imagine for example the energy profile, $e(z)$. First, an error in the dividing surface position, $\Delta z_{\rm div}$, results in an error of the interface internal energy of the form $\Delta e_{\rm int} \simeq (e_{\rm m} - e_{\rm c})\Delta z_{\rm div}$. Second, errors in the determination of the bulk values of the profile also enter in $e_{\rm int}$, namely with a factor of the length of the integration interval. Similar sources of error also hold for the interface stresses. Such errors originate mostly from small irregularities of the final profiles of density, energy and stress. Our data show that such errors do not obscure the signal of interest when calculating temperature derivatives. However, when calculating strain derivatives these errors substantially affect the derivative. We can rationalize this in the following way. On the one hand, in the case of the temperature derivatives, the three temperatures involved in the derivative calculation are all part of the same calculation, i.e. these three systems swap configurations from time to time due to the parallel tempering. Thereby small irregularities in the profiles, which do not affect the values themselves significantly, are common to all three systems, and therefore also do not show up in the differences. In that sense, parallel-tempering serves as a method for variance reduction. On the other hand, for the strain derivatives the three configurations involved in the differentiation originate from separate simulations. Therefore, small irregularities in the profiles are significant when taking differences.

The strain derivatives of the internal energy and of the interface stresses do not show a clear trend as a function of temperature, due to the problems just discussed above. Nevertheless, we would like to report the ranges of their values here for completeness: $-3\ \mathrm{J/m^2} < \pi_{xx;xx} < 0\ \mathrm{J/m^2}$, $0\ \mathrm{J/m^2} < \pi_{xx;yy} < 3\ \mathrm{J/m^2}$, $-1.5\ \mathrm{J/m^2} < \pi_{yy;xx} < 1.5\ \mathrm{J/m^2}$, $0.7\ \mathrm{J/m^2} < \pi_{yy;yy} < 1.6\ \mathrm{J/m^2}$, $0\ \mathrm{J/m^2} < e_{\mathrm{int};xx} < 0.5\ \mathrm{J/m^2}$, and $0.5\ \mathrm{J/m^2} < e_{\mathrm{int};yy} < 1.4\ \mathrm{J/m^2}$, where $\pi_{xx;xx} = \partial\pi_{xx}/\partial\epsilon_{xx}$, etc. The error bars on the stress and energy derivatives are approximately ± 0.6 and $\pm 0.3\ \mathrm{J/m^2}$, respectively.

4. Summary and discussion

We have used the method of the Gibbs dividing surface to define the interface internal energy and the interface stresses of the {201} fold surface of polyethylene. To our knowledge, it is the first time that these properties, as well as their temperature and strain derivatives, have been studied by first principles from a united-atom model. The values for the diagonal stress components $\pi_{xx} \simeq -0.27\ \mathrm{J/m^2}$ and $\pi_{yy} \simeq -0.4\ \mathrm{J/m^2}$ compare reasonably well with those inferred from experimental data. We have also discussed how the heat capacity of the entire semi-crystalline material is influenced by the internal energy of the interface and by a contribution due to phase transformation. The expression (10) for the total internal energy can be generalized to the case of many lamellar crystals, for simplicity all of cylindrical shape with the same thickness h and radius R. The total internal energy then contains two bulk contributions of the crystal and melt phase, plus two interface contributions for the fold surface and the lateral growth surface, respectively. Calculation of the 'apparent' heat capacity analogous to Eq. (11) shows the effect of the different interface contributions due to the lateral and thickness dimensions of the lamellae, which is relevant for the evaluation of experimental data.

The importance of the bulk phase properties on the interface properties has been illustrated several times, in particular when taking temperature and strain derivatives. For example, an increased pressure leads to a compaction of the interface. Therefore, a good description of the interface properties must include the bulk properties of the crystal and melt phase. These are expressed conveniently in terms of the temperatures $T_{\rm c}$ and $T_{\rm m}$ of the crystal and melt phases, respectively, and the 3×3 strain tensors $\epsilon_{{\rm c},\alpha\beta}$ and $\epsilon_{{\rm m},\alpha\beta}$, respectively, where both strain tensors are measured with respect to a reference state with stress tensor $\sigma_{\alpha\beta} = -\delta_{\alpha\beta}p_{\rm bulk}$ and $p_{\rm bulk} = 1$ atm. In the study presented here, the crystal and melt temperatures are identical, and the crystal and melt strain tensors have identical components in the xy-plane because the entire simulation cell is deformed with the same strain, as described previously. Consequently, the thermodynamic state of the interface is described exclusively in terms of the crystal and melt bulk properties, namely by the temperature $T := T_{\rm c} = T_{\rm m}$, and the

planar strain tensor described by the x- and y-components of the tensors $\epsilon_{c,\alpha\beta}$ and $\epsilon_{m,\alpha\beta}$. We expect that the commonly studied coarse-grained three component models using Helmholtz free energy expressions of the form $Af(T)$ for the interface (with A the amount of interface area) could be substantially improved by considering $Af(T,\epsilon_{c,\alpha\beta},\epsilon_{m,\alpha\beta})$ instead, in order to represent the semi-crystalline polyethylene more appropriately.

The connection between our results for the interface stresses and lamellar twist shall be discussed briefly. We do indeed measure interface stresses that are significant in that they are larger in magnitude than experimental estimates for the surface tension (with opposite sign). Also, interface stresses are known to distort the lattice spacing, as discussed in detail above. Therefore, the magnitude of these stresses can lead to twisting of the lamella, but *only if* these stresses were to occur asymmetrically at the two opposite lamella surfaces [7,8]. By construction, our simulation is symmetric about the mid-plane of the simulation, so no asymmetries are observed. Reasons for the difference between upper and lower fold surface of a lamella have to be found on different grounds. To break the symmetry, one most probably needs to look at the growth face at the same time when measuring the interface stresses.

Acknowledgements

Financial support from the Swiss National Science Foundation under Grant Number 81EZ-68591, and from the ERC program of the National Science Foundation under Grants 0079734 and EEC-9731680 (Center for Advanced Engineering Fibers and Films—CAEFF) is gratefully acknowledged.

References

[1] Cammarata RC, Eby RK. J Mater Res 1991;6:888–90.
[2] Fisher HP, Eby RK, Cammarata RC. Polymer 1994;35:1923–30.
[3] Cammarata RC, Sieradzki K. Annu Rev Mater Sci 1994;24:215–34.
[4] Wunderlich B. Macromolecular physics. New York: Academic Press; 1976.
[5] Hoffman JD. Polymer 1982;23:656–70.
[6] Calvert PD, Uhlmann DR. J Polym Sci 1973;11:457–65.
[7] Keith HD, Padden Jr. FJ. Polymer 1984;25:28–42.
[8] Lotz B, Cheng SZD. Polymer 2005;46:577–610.
[9] Rault J. J Macromol Sci Phys 1976;B12:335–71.
[10] Balijepalli S, Rutledge GC. J Chem Phys 1998;109:6523–6.
[11] Balijepalli S, Rutledge GC. Macromol Symp 1998;133:71–99.
[12] Balijepalli S, Rutledge GC. Comput Theor Polym Sci 2000;10:103–13.
[13] Gautam S, Balijepalli S, Rutledge GC. Macromolecules 2000;33:9136–45.
[14] Bassett DC, Hodge AM. Proc R Soc London 1981;A377:25–37.
[15] in 't Veld PJ, Rutledge GC. Macromolecules 2003;36:7358–65.
[16] in 't Veld PJ, Hütter M, Rutledge GC. Macromolecules 2006; 39:439–47.
[17] Paul W, Yoon DY, Smith GD. J Chem Phys 1995;103:1702–9.
[18] Rutledge GC. J Macromol Sci Phys 2002;B41:909–22.
[19] Hoffman JD, Miller RL. Polymer 1997;38:3151–212.
[20] Kofke DA. J Chem Phys 2002;117:6911–4.
[21] Neumann AW, Spelt JK, editors. Applied surface thermodynamics. New York: Marcel Dekker; 1996.
[22] Hudson JB. Surface science: an introduction. New York: Wiley; 1998.
[23] Zangwill A. Physics at surfaces. New York: Cambridge University Press; 1988.
[24] Gibbs JW. The scientific papers of J. Willard Gibbs, vol. 1. London: Longmans-Green; 1906.
[25] Herring C. Ch. 1: The use of classical macroscopic concepts in surface energy problems. In: Gomer R, Smith CS, editors. Structure and properties of solid surfaces. Chicago, IL: The University of Chicago Press; 1953.
[26] Davis GT, Eby RK, Colson JP. J Appl Phys 1970;41:4316–26.
[27] Nye JF. Physical properties of crystals. Oxford: Clarendon Press; 1985.